# Variability of cirrus cloud properties using a Polly$^{XT}$ Raman Lidar over high and tropical latitudes.

Kalliopi Artemis Voudouri[1], Elina Giannakaki[2,3], Mika Komppula[3], and Dimitris Balis[1]

[1]Laboratory of Atmospheric Physics, Physics Department, Aristotle University of Thessaloniki, Greece
[2]Department of Environmental Physics and Meteorology, Faculty of Physics, University of Athens, Greece
[3]Finnish Meteorological Institute, P.O.Box 1627, FI-70211, Kuopio, Finland

**Correspondence:** Kalliopi Artemis Voudouri (kavoudou@physics.auth.gr)

**Abstract.** Measurements of geometrical and optical properties of cirrus clouds, performed with a multi-wavelength Polly$^{XT}$ Raman Lidar, during the period 2008 to 2016 are analysed. The measurements were performed with the same instrument, during sequential periods, in three places at different latitudes, Gual Pahari (28.43°N, 77.15°E, 243m a.s.l) in India, Elandsfontein (26.25°S, 29.43°E, 1745m a.s.l) in South Africa and Kuopio (62.74°N, 27.54°E, 190m a.s.l) in Finland. The lidar dataset

5   has been processed by an automatic cirrus cloud masking algorithm, developed in the frame of this work. In the following, we present a statistical analysis of the lidar retrieved geometrical characteristics (cloud boundaries, geometrical thickness) and optical properties of cirrus clouds (cloud optical depth, lidar ratio, ice crystal depolarization ratio) measured over the three areas that correspond to subtropical and subarctic regions as well as, their seasonal variability. The effect of multiple-scattering from ice particles to the derived optical products is also considered and corrected in this study. Our results show that cirrus layers,

10  which have a noticeable monthly variability, were observed between 6.5 to 13km, with temperatures ranging from -72°C to -27°C. The observed differences on cirrus clouds geometrical and optical properties over the three regions are discussed in terms of latitudinal and temperature dependence. The latitudinal dependence of the geometrical properties is consistent with satellite observations, following the pattern observed with CLOUDSAT, with decreasing values towards the poles. The geometrical boundaries have their highest values in the subtropical regions and overall, our results seem to demonstrate that subarctic

15  cirrus clouds are colder, lower, and optical thinner than subtropical cirrus clouds. The dependence of cirrus clouds geometrical thickness and optical properties on mid temperature shows quite similar tendency for the three sites, but less variability for the subarctic dataset. Cirrus are geometrical and optical thicker at temperatures between -45°C and -35°C and a second peak is observed at lower temperatures ∼ -70°C for the subarctic site. Lidar ratio values also exhibit a pattern, showing higher values moving to the poles, with higher mean value observed over the subarctic site. The dependency of the mid temperature with the

20  lidar ratio values and the particle depolarization values is further examined. Our study shows that the highest values of cirrus lidar ratio correspond to higher values of cirrus depolarization and warmer cirrus. The kind of information presented here can be rather useful in the cirrus parameterizations required as input to radiative transfer models, and can be a complementary tool to satellite products that cannot provide cloud vertical structure. In addition, ground-based statistics of the cirrus properties could be useful in the validation and improvement of the corresponding derived products from satellite retrievals.

## 1 Introduction

Cirrus clouds are usually formed in altitudes from 6 to 14km, having an average thickness of 1.5km and temperature variability
from -80°C to -27°C (Westbrook et al., 2011). Cirrus are made predominantly, or entirely, of ice particles and the shape of their
hydrometeors varies, affected by air temperature, atmospheric pressure, and ice supersaturation (Lynch et al., 2001). Given that
30   cirrus clouds are challenging components in atmospheric and global climatological research, affecting the global radiation
budget (e.g. Campbell et al., 2016), a detailed monitoring of their properties at different geographical locations is crucial to
understand their effects on climate.

Active remote sensing techniques, such as lidar and cloud radar instruments, have proved to be useful tools in providing
continuous monitoring of high spatial and temporal distributions of cirrus clouds boundaries and their properties, and thus,
35   enhancing the opportunity of tracking cloud evolution both in time and height. The capability of a cloud radar to map vertical
and temporal structures of cloud layers has already been well recognized in the scientific community (Illingworth et al., 2007).
Additionally, elastic backscatter and Raman lidars have also been used for retrieving geometrical and optical properties of
cirrus clouds (i.e., Ansmann et al., 1992; Gouveia et al., 2017). Moreover, portable multiwavelength lidars (Polly$^{XT}$) allow for
24/7 monitoring of the atmospheric state (Engelmann et al., 2016) and can be used to establish long time series of aerosol and
40   cloud measurements. Lidar observations also allow the retrieval of detailed hydrometeor properties, such as their sphericity,
which is indicative of the shape of targets. The importance of ground-based lidar in monitoring cirrus clouds, is based on the
mapping of particularly optically thin high altitude ice clouds which cannot produce sufficient reflectivity and as a consequence
can be undetectable from cloud radars (Comstock et al., 2002) or from passive instruments. However, lidar beam attenuates
strongly in liquid water clouds, and therefore, it is likely that in the case of multiple cloud layers reliable detection of cirrus
45   clouds cannot be ensured.

In the last decades, observations of cirrus clouds properties have been conducted both in terms of field experiments (e.g.
Seifert et al., 2007) and systematic observations (e.g. Dionisi et al., 2013; Pandit et al., 2015) from groundbased lidar systems,
providing an estimation of their dependence on the geographical location. Dionisi et al. (2013) presented a methodology for
identification and characterization of cirrus clouds properties, applied to the multiwavelength Rayleigh Mie-Raman (RMR)
50   lidar in Rome. The study classified the detected cirrus clouds in different categories, based on their optical properties. Specifi-
cally, the analysis showed that 10% of the detected cirrus were subvisible clouds ($\tau < 0.03$), 49% thin ($0.03 < \tau < 0.3$) and 41%
opaque cirrus ($\tau > 0.3$). The overall mean value of cirrus optical depth was calculated $0.37 \pm 0.18$, while the mean Lidar Ratio
value (LR), corrected for multiple scattering with a constant factor, was $31 \pm 15$ sr. Another statistical analysis on optical and
geometrical properties of upper-tropospheric cirrus clouds based on a lidar dataset, was conducted in Amazonia (Gouveia et
55   al., 2017). The frequency of occurrence of cirrus clouds classified as subvisible was 41.7%, whilst 37.8% was for thin cirrus
and 20.5% for opaque cirrus. The correction of the multiple scattering effect to the optical products in this study was made
following the model of Hogan (2008). Lakkis et al. (2015) revealed that the most commonly observed cirrus were characterized

as optically thin cirrus, rather than opaque ones, with a mean optical depth value of $0.26 \pm 0.11$, over Buenos Aires (34.6°S, 58.5°W). There is also a number of satellite based studies from either lidar (Cloud-Aerosol Lidar with Orthogonal Polarization (CALIOP), Dupont et al., 2010) or cloud radar (Cloud Profiling Radar (CPR)) or combined lidar and cloud radar (e.g. Sassen et al. 2008) retrievals that provide a global view concerning the seasonal frequencies of cirrus clouds and their geometrical and optical properties and their variabilities.

However, there are only few long-term studies based on ground-based lidar systems, while these have a limited geographical distribution. This kind of observations that correspond to different areas and atmospheric conditions are crucial to reveal information of the latitudinal dependence of the cirrus properties and can provide indications about the aerosol effect on the geometrical and optical characteristics of the detected cirrus layers. On top of that, these observations can be further used in the validation and improvement of the satellite retrievals, which provide global distribution of cirrus clouds (Sassen et al., 2008). Given that for satellite retrievals, the main input parameter to the optical processing of the cirrus layers is the lidar ratio, the selected lidar ratio value can introduce errors on the retrieved extinction and optical depth values of the cirrus layers, as it is illustrated by Young et al., (2018). The optical depth comparison of the Version 4.10 (V4) of the CALIOP optical depths and the optical depths reported by MODIS collection 6 shows substantial improvements relative to earlier comparisons between CALIOP version 3 and MODIS collection 5, as a result of extensive upgrades of the extinction retrieval algorithm. New apriori information of the lidar ratio value for the cirrus layers, included in Version 4.10 (V4) of the CALIOP data products, led to improvements of the extinction and optical depth estimates of the cirrus cloud layers. Thus, ground based lidar observations of the cirrus properties, that correspond to different areas and atmospheric conditions, are crucial to verify and eventually improve the satellite retrievals.

The aim of this work is to retrieve and analyze the cirrus geometrical, intensive and extensive optical properties at different latitudes (subtropical and subarctic), from observations derived with the same ground based lidar system, which partly fills the gap concerning the latitudinal coverage of existing ground-based lidar studies. Then the observed differences are discussed in order to identify the possible causes. The information of the lidar ratio is an important parameter for the inversion of lidar signals in instruments that do not have Raman channel and space-based lidars, such as CALIPSO (Cloud-Aerosol Lidar and Infrared Pathfinder Satellite Observations), that depend on a parameterization that may vary with location. Thus, information provided by well-calibrated ground based measurements is quite critical. Analysis of the lidar ratios values derived from lidar measurements in different parts of the world, where different atmospheric and aerosol conditions prevail, will provide results that are more representative of the actual conditions and thus their use will lead to reductions in the uncertainties of the satellite retrievals.

The manuscript is structured as follows: after a brief description of the portable lidar system (Polly$^{XT}$) and the measuring sites in Section 2, we present the data analysis algorithm and the methods applied for the optical products retrievals in Section 3. The lidar derived statistical analysis and seasonal variations of geometrical and optical properties of cirrus clouds in both subtropical and subarctic areas over the period 2008-2016 are presented and discussed in Section 4. Concluding remarks are presented in Section 5.

## 2 Instrument and Measuring Sites

A multi-wavelength depolarization Raman lidar Polly$^{XT}$ of the Finnish Meteorological Institute (FMI) performed automated measurements during the period 2008-2016 in three different geographical regions. The system is based on a compact, pulsed Nd:YAG laser, emitting at 355, 532 and 1064 nm, at 20 Hz repetition rate. The laser beam is pointed into the atmosphere at an off-zenith angle of 5°, so the impact of the specular reflection by ice crystals into cirrus layers on the backscattered signals is negligible. The backscattered signal is collected by a Newtonian telescope, with 0.9m focal length. The vertical resolution of the signal profiles is equal to 30m and the temporal resolution is 30s. The setup of the system includes two Raman channels at 387 and 607 nm, three elastic channels at 355, 532 and 1064 nm, a depolarization channel at 355nm (for India and South Africa), a depolarization channel at 532nm (cross-polarization with respect to the initial emitted polarization plane) for Kuopio and a water vapour channel at 407nm. A brief description of the system components is presented in Table 1, while a detailed description is provided in Althausen et al., (2009) and Engelmann et al., (2015). All measurements processed within the period 2008-2016 are available online at http://polly.tropos.de.

The Polly$^{XT}$ has participated in two campaigns in two subtropical areas, within the framework of the EUCAARI (European Integrated project on Aerosol Cloud Climate and Air Quality interactions) project (Kulmala et al., 2011), covering a wide range of cloud types. Measurements have been performed in Gual Pahari (28.43°N, 77.15°E, 243m a.s.l) in India from March 2008 to March 2009 (Komppula et al., 2012), and in Elandsfontein (26.25°S, 29.43°E, 1745m a.s.l) about 150km from Johannesburg in South Africa from December 2009 to January 2011 (Giannakaki et al., 2015). Figure 1 presents the map of the three measuring sites. Measurements in Gual Pahari were not performed continuously from March 2008 to March 2009. Due to technical problems with the laser, the data coverage from September to January was limited. Measurements were not performed in October 2008 and January 2009, and in September and November-December only a few usable profiles were measured (Komppula et al., 2012). Measurements in Elandsfontein were performed almost continuously, as two periods were dedicated to the maintenance of the system (the one from December 23rd to January 26th 2009 and the second one, from October 23rd to November 23rd 2010). Since November 2012 the Polly$^{XT}$ is operating in Kuopio (62.74° N, 27.54°E, 190m a.s.l) in Finland providing continuous measurements of aerosols and clouds (Filioglou et al, 2017).

## 3 Geometrical and optical retrievals of cirrus clouds

### 3.1 Description of the cirrus retrieval algorithm

Several steps were followed for the processing of the signal at 1064nm derived by the Polly$^{XT}$, needed for the estimation of the cirrus boundaries. These are illustrated in Figure 2. Firstly, the signal to noise ratio (SNR, Eq. 1) is calculated according to the following equation (Georgousis et al., 2015):

$$SNR = \frac{Csig}{\sqrt{Csig+Cbg}} \tag{1}$$

where $C_{sig}$ represents the raw lidar signal and $C_{bg}$ represents the background correction. The SNR is selected above 3.5, since the lidar signal is strongly attenuated at higher altitude levels and the noisy parts of the signal should be rejected (above the selected threshold, boundary layers estimation found independent from SNR). Then, we subtract the zero and background levels and we calculate the range-corrected signal (P(z)). In the next step, we normalize the range-corrected signal by its maximum value below 1.5km. Given that lidar signals are uncalibrated and signal levels from one lidar system to another can be rather different, the normalization ensures the applicability of the criteria used by Baars et al. (2008).

After the above corrections, the Wavelet Covariance Transform (WCT) is applied to the range corrected signal. The method (Eq. 2), detects discontinuities in the lidar signal, such as the top of the boundary layer, elevated aerosol layers or cloud boundaries, allowing the detection of cirrus cloud base and top (Brooks, 2003).

$$WCT = \sum_{b-\frac{\alpha}{2}}^{b} P(z)z^2 dz - \sum_{b}^{b+\frac{\alpha}{2}} P(z)z^2 dz \qquad (2)$$

In eq. (2), WCT is the result of the transformation, P(z) is the range corrected profile, z is the altitude, b is the height at which a noticeable change in the normalized signal occurs, and $\alpha$ is the dilation chosen. A critical step to the accurate WCT application on the signal is the selection of an appropriate value of the window (dilation), so as to distinguish cloud layers from aerosol layers. In our case, a dilation of 225m, is chosen, proportional to the cirrus geometrical depth (Baars et al., 2008). Another critical step is the threshold WCT value for the determination of the cirrus boundary. A threshold value of 0.1 is selected as a detection limit for both the base (-0.1) and the top (+0.1) of cirrus cloud (Baars et al., 2008) after sensitivity studies. The WCT transformation has already been applied successfully on cirrus cloud detection (Dionisi et al., 2013).

An hourly lidar measurement of a cirrus case is defined in this study as follows: To calculate the cirrus boundaries, the wavelet covariance is calculated for every single profile (every 30s) and a mean value of the cirrus base and top are attributed to the one-hour processing. We also consider the differences within an hour between the bases/top calculated should not exceed the 0.5km. With this assumption, we exclude cases with large variability of cirrus layers.

Finally, cloud retrievals from the algorithm are classified as cirrus clouds when the following four criteria were met: i) the particle linear depolarization value is higher than 0.25 (Chen at al., 2002; Noel et al., 2002), ii) the altitude is higher than 6km, iii) the base temperature is below -27°C (Goldfarb et al., 2001; Westbrook et al., 2011) and iv) the top temperature is below -38°C (Campbell et al., 2015). The application of these criteria is made so as to avoid the presence of liquid water. It should be pointed out that lidar measurements were processed only in the absence of lower tropospheric (below 4 km) thick clouds.

The application of the WCT on a case of cirrus layer observed on July 20th 2016 at Kuopio station, for a time period between 00:00 and 01:00 UTC is presented. The hourly mean wavelet applied to the corrected 1064 signal and the hourly mean particle depolarization ratio and the backscatter coefficient profile of the cirrus evolution are presented in Fig. 3. The temperature values are also plotted with white line and the threshold values are marked with red lines.

## 3.2 Retrieval of the optical properties of cirrus

The integration of the extinction profile (a) between the defined cloud base ($z_{base}$) and the top of the cirrus layer ($z_{top}$) is calculated to obtain the cirrus optical depth (COD) from the lidar measurements as shown in Eq. (3).

$$155 \quad COD = \int_{z_{base}}^{z_{top}} a(z)dz \qquad\qquad (3)$$

The night-time measurements from Polly$^{XT}$ were processed by the Raman method, which allows the independent determination of the extinction and backscatter coefficients, thus providing the lidar ratio (extinction-to-backscatter ratio) (Ansmann et al., 1992). For the retrieval of the cirrus extinction coefficient profiles obtained from the daytime measurements, the integration of the backscatter profile multiplied by the lidar ratio is calculated. The daytime measurements from Polly$^{XT}$ were processed
160 using the Klett inversion (Klett, 1981; Fernald, 1984), with respect to the ratio of the extinction to the backscatter coefficient. These two unknowns have to be related using either empirical or theoretical methods in order to be able to invert the lidar equation. In our study, the lidar ratio was determined by comparing the forward and the backward solution of Klett and the lidar ratio value was chosen as the value for which the aforementioned profiles tend to coincide (Ansmann et al., 1992).

The calculation of the corresponding molecular backscatter and extinction profiles was made based on temperature and
165 pressure profiles obtained from radio soundings at each site. Radiosonde observations released at Safdarjung Airport (28.58°N, 77.20°E) in New Delhi, India twice a day, radiosondes from Upington International Airport (28.40°S, 21.25°E), in South Africa and radiosondes launched daily at 06 and 18 UTC at the Jyvaskyla Airport, located to the southwest (62.39°N, 25.67°E) of the lidar station at Kuopio, were used. Mid-temperature is also calculated in our study. Mid remperature is defined as the mean temperature between the temperature at base and temperature at top altitude for each cirrus layer.

170 Another important lidar quantity to be calculated is the particle depolarization ratio, which constitutes a qualitative way to discriminate particle shapes and to distinguish spherical from non-spherical particles. The calibration of the depolarization measurements, needed for the calculation of the particle depolarization ratio, was determined by using the geometric mean of the two $\pm45°$ measurements, following the procedure described by Freudenthaler et al., (2009). The particle depolarization ratio is presented only for the dataset of Kuopio, as for the other two sites only the Rayleigh calibration method for the
175 calibration measurements was available.

## 3.3 Multiple scattering correction on optical products

The lidar equation assumes single scattering from the hydrometeor, but eventually the received photons could have been scattered multiple times before reaching the telescope. This effect, named multiple scattering, is considerably important primarily to the measured extinction coefficient values of cirrus clouds, and secondly to the calculated cirrus optical depth and the esti-
180 mated lidar ratio values. Multiple scattering depends not only on cloud optical depth and cloud extinction, but also on the lidar system components, such as the laser beam divergence and the full-angle field-of-view of the receiver.

The relative influence of multiple scattering decreases with increasing height within the cloud, and the errors of the extinction coefficient can be even equal to 60% at the cirrus base (Lynch et al., 2001). As generally, multiple scattering effect cannot be negligible in a receiver field of view equal to 1mrad (Wandinger, 1998), this effect on cirrus clouds optical properties was considered. In order to calculate the multiple scattering contribution to the calculated optical products, the Eloranta model (Eloranta, 1998) was used to estimate the ratio between the total received power and the contribution of the single scattering, the ratio $P_{tot}(z)/P_1(z)$ (Eq. 4). The measured extinction coefficient $a_{eff}$ is then related to the actual (single scattering) coefficient a(z) through the parameter F as shown in Eq. (5) (Wandinger, 1998).

$$F(\lambda,z) = \frac{\frac{d}{dz}ln\frac{P_{tot}(z)}{P_1(z)}}{2a_{eff}(\lambda,z) + \frac{d}{dz}ln\frac{P_{tot}(z)}{P_1(z)}} \tag{4}$$

$$a(\lambda,z) = \frac{a_{eff}(\lambda,z)}{1 - F(\lambda,z)} \tag{5}$$

The model assumes hexagonal ice crystal shapes and the required inputs are: (i) the laser beam divergence, (ii) the receiver field of view, (iii) the cirrus effective radius, (iv) the measured single scattering extinction profile (or the lidar ratio multiplied by the backscatter for the daytime measurements) and (v) the order of scattering. The estimation of the cirrus effective radius was taken from Wang and Sassen (2002), based on the linear relation of the effective radius with the cirrus cloud temperature derived from radio soundings. For the multiple scattering calculation, the code applies an iterative method including the following steps:

i) The measured extinction profile of the cirrus layer is provided ($a_{eff}$).

ii) With the provided effective radius profile of the cirrus layer and the measured extinction coefficient, an iterative procedure provides the ratio $P_{tot}$(z)/$P_1$(z).

iii) From (ii) a first value for the correcting factor F(z) can be found.

iv) The iterative procedure continues till the calculation of a stable correcting factor F(z).

v) The corrected extinction can be then calculated from equation (5) and hence the value of lidar ratio.

The model has already been validated against other models (Hogan, 2006) and has already been applied in cirrus lidar applications (Giannakaki et al. 2007). In the following sections, the cirrus optical properties (lidar ratio, extinction coefficient, and optical depth) derived in the frame of this study were corrected for multiple scattering.

## 4 Results and discussion

In the following section, we present the mean geometrical and optical properties of the detected cirrus layers within the period 2008-2016 for the three measurement sites, which correspond to subtropical and subarctic regions, and we further discuss the differences between the retrieved properties.

## 4.1 Cirrus cloud cover detection

As cirrus detection in our study we refer to only lidar determined cirrus cases, as these are described in paragraph 3.1 and thus can not be representative of the general seasonal patterns of cirrus occurrence for the areas under study. Generally, Polly$^{XT}$ measured almost continuously (24/7) under favor weather conditions and the profiles that fulfil the criteria for a cirrus detection are hourly averaged, so the pattern presented (not shown) is only an indication and biased by the presence of low clouds and rain. During the one-year-long measurement period over Gual Pahari, Polly$^{XT}$ was measuring on 183 days, corresponding to 2500h in total. The time periods with technical issues (mentioned above) and the occurrence rate of low clouds observed between March and September leaded to a limited dataset of cirrus observations. Thus, the detected cirrus clouds cannot provide any monthly trend and cannot be representative of an annual pattern. Concerning the annual pattern observed over Elandsfontein, a total measurement time of about 4935h corresponding to 88 cirrus profiles have been obtained, during the observation period between 11 December 2009 and 31 January 2011, with the exception of the two periods of maintenance of the system (mentioned above). The maximum detection of cirrus layers is reported during May and December. No data processing could be performed during unfavourable weather conditions, such as the presence of low cloud, observed mainly the months between January to April with a percentage of $\sim 30\%$ of the total measurement period. The analysis of measurements over Kuopio showed that the cirrus cloud cover is found to vary both diurnally and seasonally. From the available data, the detection of cirrus clouds appears to exhibit an annual pattern with the maximum detection from February to September and minimum occurrence during the period between October and January, given the favorable meteorological conditions. Layers of low water clouds were present all year long, with the peak of monthly occurrence between April (28 cases) and November (27 cases). This monthly pattern of low clouds existence seems to follow the annual temperature cycle over the region (Jylha et al., 2004), with maximum temperature values observed during the period April to October. Concerning the diurnal pattern, the number of detected cirrus clouds during nighttime is higher from March to Semptember, and lower in the period from October to January.

## 4.2 Geometrical properties of cirrus clouds over the sub-arctic and tropical sites

Mean cirrus cloud geometrical thickness reported in literature from satellite retrievals is about 2.0 km globally (Sassen et al., 2008), while a broad distribution of geometrical boundaries from ground-based systems have been reported in literature (e.g., Gouveia et al., 2017; Seifert et al., 2007; Hoareau et al., 2013). Figure 4 shows the monthly variations of the cirrus base and top height (displayed in monthly boxplots) derived with the automated algorithm, along with the corresponding mean temperatures above each site. The cirrus geometrical properties show a broad monthly distribution ranging from 6790m to 13070, having the larger variability in the two subtropical sites compared to the subarctic site.

The cirrus lidar dataset in Gual Pahari (28.43°N, 77.15 °E,243m a.s.l - Northern hemisphere) region is the less extensive one compared to the other two sites and limitations due to the low signal to noise ratios exist. Indeed the sampling might not be statistically representative of the cirrus cloud properties, but some first results can be discussed. The mean value of cirrus base is calculated $9000 \pm 1580$m, whilst mean top is found to be $10600 \pm 1800$m, with mean geometrical thickness of $1500 \pm$

700m. The temperature varies from -27°C to -50°C. Our results are consistent with another study over North China (Min et al., 2011), based on CALIOP satellite measurements. In this study a value of 1600 ± 1015m is reported for the cirrus geometrical thickness. According to this study, the cirrus top temperatures were found lower than -50°C and higher than -80°C. From the cirrus profiles processed over Elandsfontein (26.25°S, 29.43°E, 1745m a.s.l - Southern Hemisphere), the mean value of cirrus base is calculated to be 9200 ± 810m, while mean top at 10826 ± 906m and the mean geometrical thickness is 1626 ± 735m. For the sub-arctic station of Kuopio (62.74°N, 27.54°E, 190m a.s.l), the seasonal mean cirrus cloud-base heights are calculated as follows: 8363 ± 1169m (MAM), 8326 ± 1120m (JJA), 9173 ± 1100m (SON), and 8900 ± 1390m (DJF) with an annual mean value of 8600 ± 1080m. The annual mean of the upper boundary of cirrus layers is 9800 ± 1075m, with a maximum value of 12595m during April. The mean geometrical thickness is calculated to be 1200 ± 700m. Base cirrus temperatures range from -71°C to -27°C having a mean value of -43°C. The corresponding temperature values of the top, range from -72°C to -38°C, with a mean value of -57°C. These values are in accordance with the corresponding ones from the combined data of CloudSat and CALIPSO measurements (Sassen et al., 2008).

Table 2 summarizes the mean geometrical values calculated for each site separating daytime and nighttime measurements. The averaged geometrical properties between daytime and nighttime are found to be nearly identical above all sites, with differences less than 0.3km.

## 4.3  Optical properties of cirrus clouds over the sub-arctic and tropical sites

This section presents the cirrus optical properties for the three regions and Figure 5 shows the monthly variations of the cirrus optical properties (displayed in monthly boxplots) above each site.

The COD values over the three sites are presented in Figure 5a and 5b. For the subtropical region of Gual Pahari the mean COD at 355nm is 0.59 ± 0.25 and the mean COD at 532nm is found to be 0.45 ±0.30. The classification of clouds according to Sassen and Cho (1992), shows that the detected cirrus layers are classified as follows: sub-visible cirrus (0%), optical thin cirrus (20%) and opaque cirrus (80%). One possible reason for the absence of subvisible cirrus clouds in this dataset can be the lower SNR that does not allow detectability of optically thin clouds at Gual Pahari. Another study over North China (Min et al. 2011), reported a mean value of optical depth of 0.41 ± 0.68 at 532nm and the classification of the detected cirrus layers was made as follows: subvisible cirrus (30.26%), optical thin (34.59%) and opaque cirrus (21.54%). He et al. (2013) in his study over the region reported that the optical depth of the cirrus layers varied between 0.0004 and 2.6, with a mean value of 0.33. For the subtropical region of Elandsfontein the mean value of COD at 355nm is calculated at 0.35 ± 0.03 and the mean COD at 532nm is found to be 0.30 ± 0.30. The COD have their highest values between April (1.36) and May (1.33) and December (1.02) and the percentage of 2% is categorized as subvisible cirrus, 61% as thin cirrus and 37% as opaque cirrus. For the Kuopio, the column-integrated mean corrected COD at 355nm is 0.25 ± 0.2, and is found to vary between 0.018 and 1.53, while the mean COD at 532nm is found to be 0.24 ± 0.20. The highest values of COD are found between January and March, with the highest value of 0.95. The mean COD at 355nm calculated in this study is larger than the value of 0.16 ± 0.27 reported by Das et al. (2009) and smaller than the value of 0.41 ± 0.68 reported by Min et al. (2011) from midlatitude observations. A number of other studies have reported mean COD values between 0.2 and 0.4 (Gouveia et al., 2017). The

classification of the cirrus clouds according to Sassen and Cho (1992) indicates that 3% of the cirrus measured over Kuopio are subvisible ($\tau < 0.03$), 71% are thin cirrus ($0.03 < \tau < 0.3$) and 26% are opaque cirrus ($\tau > 0.3$). The low percentage of the subvisible category of cirrus layers, have also been observed over midlatitude sites (e.g., Kienast-Sjogren et al., 2016), where subvisible cirrus clouds have been measured during 6% of the observation time.

In what follows we examined if there is potential connection between the COD values derived in the different sites and the free tropospheric AOD load over the regions which are exposed to different aerosol sources. Table 4 lists the predominant aerosol type over each region and the results from the analysis of AOD at 355 nm in the free troposphere and the calculated COD values. We can not reach to any conclusion, only report an indication of the relationship of the aerosol load on the derived cirrus statistics, as the higher AOD values are linked with the higher COD values calculated for the two subtropic regions. More specifically, the one year aerosol analysis of lidar observations in Gual Pahari (Komppula et al., 2012) showed a distinct seasonal pattern of aerosols, with aerosol concentrations slightly higher in summer (June - August) compared to other seasons, and particles larger in size. During the summer and autumn, the average lidar ratios were larger than 50 sr, suggesting the presence of absorbing aerosols from biomass burning. The lidar observations that were performed at Elandsfontein and used for aerosol characterization for the corresponding study period (Giannakaki et al. 2016) showed that the observed layers were classified as urban / industrial, biomass burning, and mixed aerosols. The analysis showed that the more absorbing (higher lidar ratio at 355 nm) biomass particles were larger on August and October, while the category of Urban/industrial had their peak on January, March and May. From the other hand, cirrus observations had their peak from March to May, with a second peak on August. Kuopio is an urban area and constitutes a low aerosol content environment. The columnar analysis of sunphotometer observations (Aaltonen et al., 2010) revealed that the high Angstrom exponent values observed can be possible linked with the presence of fine particles, while the seasonal analysis of the optical depth showed that there is no significant variation.

Concerning the lidar ratios values (Figure 5c and 5d) observed over Gual Pahari, the lidar ratio value at 355nm is calculated at $27 \pm 12$ sr and the corresponding one for 532nm is $28 \pm 22$ sr and the lidar ratios reach their highest values on May. Our results are in agreement with another cirrus cloud study for the area; He et al. (2013) report a mean lidar ratio value of 28 sr, using a micropulse lidar. For the Elandsfontein site, the mean LR at 355nm value is found to be $26 \pm 6$ sr and the mean LR at 532nm is $25 \pm 6$ sr and the lidar ratios reach their highest values during April. A mean value lidar ratio of $33 \pm 7$ sr at 355nm is observed for the whole period studied over Kuopio site, with higher variability observed on June, while the corresponding mean value LR at 532nm is calculated to be $31 \pm 7$sr, without any obvious seasonal cycle. Specifically, the mean LR at 355nm for the corresponding months are calculated as follows: $33 \pm 7$ sr (MAA), $34 \pm 7$ (JJA), $33 \pm 7$ (SON) and $34 \pm 5$ (DJF). For opaque, thin and sub-visible cirrus clouds the means are $31 \pm 6$ sr, $34 \pm 7$ sr, and $35 \pm 7$ sr, respectively. Gouveia et al. (2017) found a mean LR at 355nm value of $23.9 \pm 8.0$sr (SD) for the tropical region of Amazonia, while Giannakaki et al., (2007), reported a corresponding value of $30 \pm 17$sr for a mid-latitude station. Josset et al. (2012) and Garnier et al. (2015) analyzed spaceborne CALIOP observations. Both studies concluded that cirrus lidar ratio (corrected for multiple scattering effects) around the globe has typically values of 30-35sr $\pm$ 5-8sr at 532 nm.

Concerning the monthly variability of the depolarization values (Figure 5e) over Kuopio, no clear tendency is observed. The higher monthly mean value is observed on July, but the variability is less than 0.04 between months, with a mean value of 0.38 ± 0.07.

As the assumption that the backscatter and extinction coefficients for sufficiently large cirrus particles are spectrally independent; the color ratio (ratio of backscatter profiles, CR) at 355nm and 532nm is supposed to be equal one. This assumption is also used in satellite processing schemes. However, it is reported that the measured variability of cirrus color ratios is much larger than previously realized and that measured color ratios are higher in the tropics (Vaughan et al., 2010). For the Kuopio station, mean CR is found 1.1 ± 0.8, while for the less extensive dataset of New Delhi the mean value is found 1.5 ± 0.8 and for Elandsfontein the mean value is 1.4 ± 1.1.

In Figure 6, we further examine the dependence of the LR at 355nm with the COD at 355nm values on intervals of 5 sr. The dashed lines indicate the categories defined by Sassen and Cho (1992). The most common lidar ratio values from 25 to 40 sr are found for quite low COD values (corresponding to thin cirrus) for the subarctic station.

Table 3 summarizes the mean optical values discussed above, for the three sites, separating daytime and nighttime observations. Generally, the averaged optical properties values are found to be nearly identical, except one site (New Delhi), where average nighttime optical properties found higher (∼ 4sr) than that of daytime.

## 4.4 Cirrus classification at Kuopio

Additional analysis on each cirrus category (according to Sassen and Cho, 1992) is also conducted for Kuopio site as measurements in this station represent the most extensive dataset between November 2012 and December 2016.

### Category "Subvisible"

Subvisible cirrus are geometrical thin layers with mean geometrical thickness of 643 ± 211 m. Generally, subvisible cirrus detection is a challenging component in satellite retrievals. MODIS, for example, is not sensitive to optically thin cirrus clouds due to the insufficient contrast with the surface radiance (Ackerman et al., 2008; Ackerman et al., 2010), while the CALIPSO and CloudSat observations are more sensitive to the height and presence of subvisible and thin cirrus (Hong et al., 2010). Thus, the mapping of subvisible cirrus can be rather important in climatological studies. In our study, 6 cases of cirrus with COD less than 0.03 are analyzed, mostly detected during February. Subvisible cirrus geometrical thickness found 750 ± 269 m, less than the mean value of all cirrus clouds, and their temperature 2°C-3°C colder than the mean temperature. These values are consistent with previous studies of subvisible cirrus from spaceborne lidar observations, examined on a global scale (Martins et., 2011). Their mean COD at 355nm is calculated 0.021 ± 0.0031, their mean LR at 355nm is 34 ± 7sr and their mean particle depolarization value is 0.45.

### Category "Thin"

As mentioned previously, thin cirrus is the most predominant type of cirrus in our study, with 152 observations. Thin cirrus can also be undetectable by passive remote-sensing satellites, especially the ones with COD less than 0.2, and have so far

not systematically been characterized. Their geometrical thickness found to be $1100 \pm 586$ m. Their mean COD at 355nm is calculated $0.16 \pm 0.07$, their mean LR at 355nm is $34 \pm 7$ sr and their mean particle depolarization value is $0.3 \pm 0.13$.

**Category "Opaque"**

Opaque cirrus are the one with the highest value of optical depth that contribute the most on the total radiative forcing (Kienast-Sjogren et al., 2016). In our study, a total of 55 measurements of opaque cirrus are processed. Their mean geometrical thickness is found to be $1462 \pm 659$ m, higher than the value of all cirrus categories. Their mean COD at 355nm is calculated $0.5 \pm 0.21$, their mean LR at 355nm is $31 \pm 6$ sr and their mean particle depolarization value is $0.33 \pm 0.12$.

## 4.5 Latitudinal and temperature dependence of cirrus properties

In this section we firstly examine the latitudinal dependence of the cirrus geometrical and optical properties. The reported values in literature from previous studies based on lidar grounbased dataset and the retrievals of the current one are listed on Table 5 and plotted in Figure 7 for comparison. We can note, that the cirrus geometrical properties and the lidar ratio values may vary greatly depending on the latitude and a decreasing trend of the geometrical boundaries with the rise of the distance from the equator is obvious from the groundbased studies. This pattern is in accordance with the Cloudsat observations (Sassen et al., 2008). The derived cirrus cloud geometrical properties, based on the satellite information, peaks around the equator and at midlatitudes sites, with generally decreasing amounts as the poles are approached. In our study, cirrus layers have been observed up to altitudes of 13km above the subtropical sites, whereas they have only been detected to about 1km lower at the subarctic region, following the above pattern. On the other hand, the lidar ratio values seem to follow a diverse relation, showing greater values moving to the poles. In our study, lower LR values are observed for Gual Pahari and Elandsfontein and higher mean value for Kuopio. Overall, our results seem to demonstrate that subarctic cirrus clouds are colder, lower and optical thinner than subtropical cirrus clouds. However, a more extended database is needed to strengthen these indications.

The dependence of geometrical and optical properties on mid-cirrus temperature is also examined in Fig. 8. In order to investigate this dependence, we have grouped cirrus clouds temperatures into 5°C intervals. The number of cases per temperature bin are also labeled. Temperature values are obtained from radio soundings, as mentioned above. Thicker clouds ($\sim 1.5$ km) are observed at temperatures between $\sim$ -45°C and $\sim$ -35°C, with decreasing thickness reported for lower temperatures, for both the subtropic and subarctic regions and a second peak is found in the range between $\sim$ -75°C and $\sim$ -65°C for the subarctic station. A similar trend has been reported for a midlatitude region by Hoareau et al. (2013), where thickest cirrus layers were found about -42.5°C, and thinner ones at both colder and warmer temperatures. Another study (Pandit et al., 2015) reports that the geometrical thickness increases from 1 to 3.5 km as mid-cloud temperature increases from -90 to -60°C, while for the further increase in temperature from -60 to -20 °C, the geometrical thickness decreases to less than 1 km. Concerning the optical properties shown in Fig. 8, a steady increase of lidar ratio from -25°C to -40°C is noticed for the two subtropical stations, while the variability of this parameter is relatively constant across months for the subtropic station, with a slightly increase at warmer temperatures (Figure 10b). There are indications that the cloud optical depth increases with the increasing cirrus mid temperature for the two subtropical sites (Fig. 10c). At cold temperatures ($\sim$ -65°C), optical thickness for cirrus

layers of the subarctic station is high, compared to warmer temperatures and also cloud thickness for this temperature is similar high ( ∼ 1.5 km). The dependence of the particle depolarization values on base temperature is also examined (Fig. 8d). No clear tendency is found, as the variability of this parameter is relatively constant, with a slightly increase of the particle depolarization with the increasing mid temperature. This behaviour indicates a relation between cirrus ice crystal shape and temperature, however, more studies should be done in order to examine this behavior on various geographical locations.

Figure 9 presents the color ratios values on 5°C intervals of cirrus mid temperature, indicating an almost stable behavior with temperature. Generally, we can conclude that for higher altitudes, lower spectral dependence is noticed, taking also into account the number of measurements performed at each site.

The dependency of the mid temperature with the lidar ratio values at 355nm and the particle depolarization values is further examined (Figure 10). Fig. 10 shows that the highest values of cirrus lidar ratio (>40) correspond to higher values of cirrus depolarization (>0.4) and warmer cirrus. Moreover, it can be seen the variety of depol values that correspond to the mean value of lidar ratio (∼ 31). A similar behavior is reported in Chen et al. (2002) for lidar ratio values higher than 30 sr. In his study, the relationship between the depolarization ratio and the lidar ratios shows the former split into two groups for lidar ratios higher than 30. The first group has high depolarization ratios about 0.5 and the second one has 0.2.

## 5 Conclusions

Observations of cirrus clouds geometrical and optical properties, performed with a ground-based multi-wavelength Polly$^{XT}$ Raman Lidar, during the period 2008 to 2016 are analyzed and presented in this study. The measurements were performed in three places at different latitudes, Gual Pahari (28.43°N, 77.15°E, 243m a.s.l) in India, Elandsfontein (26.25°S, 29.43°E, 1745m a.s.l) in South Africa and Kuopio (62.74 °N, 27.54°E, 190m a.s.l) in Finland and an algorithm is developed to automatically define the cirrus cloud boundaries.

The statistical behaviour of the cirrus clouds properties in the different geographical and climatic counterparts shows that the geometrical boundaries display large distribution for the two subtropical regions with higher values of geometrical thickness, with mean thickness of $1500 \pm 700$m, $1600 \pm 735$m and $1200 \pm 700$m for Gual Pahari, Elandsfontein and Kuopio respectively, showing their dependence on the geographical location. The corresponding overall mean value of COD at 355nm is calculated to be $0.60 \pm 0.25$ and $0.35 \pm 0.30$, for Gual Pahari and Elandsfontein correspondingly, while a slightly lower mean of $0.25 \pm 0.2$ is calculated for Kuopio. The lidar ratio values at 355nm show higher values moving to the poles, with calculated values to be $27 \pm 12$ sr, $26 \pm 6$ sr, and $33 \pm 7$ sr for Gual Pahari, Elandsfontein and Kuopio, respectively. Overall, our results seem to demonstrate that subarctic cirrus clouds are colder, lower, and optical thinner than subtropical cirrus clouds. However, a more extended database is needed to strengthen these indications.

The dependence of cirrus clouds geometrical thickness and optical properties on mean temperature is also examined, showing quite similar tendency, but less variability for the subarctic dataset. The dependence of cirrus clouds geometrical thickness and optical properties on mid temperature shows quite similar tendency, but less variability for the subarctic dataset. Cirrus found geometrical and optical thickest at temperatures between -45°C and -35°C. At temperatures below -55°C, the optical thickness

of cirrus layers becomes again high and this trend appears only for the subarctic station. However, we should keep in mind that the number of samples corresponding to temperatures below -60°C is limited. The lidar ratio is found to be quite constant with temperature, with a slightly increase in the warmer mid temperatures, showing larger variability for the subtropic datasets, while the particle depolarization values seem almost constant at temperatures between -27°C and -60°C.

The geometrical and optical properties of cirrus layers are studied in detail, providing information useful in the validation of the cirrus parameterizations in models. Furthermore, our results could be useful for lidar ratio selection schemes needed by satellite optical properties retrievals of cirrus layers over different locations, e.g., the upcoming EarthCARE (Earth Cloud Aerosol and Radiation Explorer) mission. The spectral dependence discussed above, is another important issue for the satellite algorithm schemes, given the different wavelengths applied among the different satellites.

In any case, further cirrus observations must be conducted, so as to investigate whether differences in the background aerosol load contribute to potential differences in the cirrus cloud geometrical and optical properties and which are the different atmospheric mechanisms leading to these differences over the different regions.

*Author contributions.* KA. Voudouri prepared the automatic algorithm for the cirrus detection and processed the lidar measurments for the optical retrievals during the period 2008-2016. KA. Voudouri prepared the figures of the manuscript. E. Giannakaki reviewed parts of the results. M.Komppula is the PI of the lidar station and D. Balis directed the preparation of the manuscript. KA. Voudouri prepared the manuscript with contributions from all co-authors.

*Competing interests.* The authors declare that they have no conflict of interest.

*Acknowledgements.* This work has been conducted in the framework of EARLINET (EVR1 CT1999-40003), EARLINET ASOS (RICA-025991), ACTRIS, and ACTRIS-2 funded by the European Commission. The research leading to these results has received funding from the European Union's Horizon 2020 research and innovation program under grant agreement no. 654109 and previously from the European Union Seventh Framework Programme (FP7/2007-2013) under grant agreement no. 262254. This work was partly funded by the European Commission 6th Framework under the European Integrated Project on Aerosol Cloud Climate and Air Quality Interactions, EUCAARI. Voudouri K.A acknowledges the support of the General Secretariat for Research and Technology (GSRT) and Hellenic Foundation for Research and Innovation (HFRI). (Scholarship Code: 95041).

# References

435    Aaltonen, Veijo & Rodriguez, Edith & Kazadzis, Stelios & Sogacheva, Larisa & Arola, Antti & de Leeuw, Gerrit.: Characteristics of the aerosol climatology over Finland based on the optical columnar properties. 12. 10788, 2010.

Ackerman, S., Holz, R., Frey, R., and Eloranta, E.: Cloud Detection with MODIS: Part II Validation, J. Atmos. Ocean. Tech., 25, 1073-1086, doi:10.1175/2007JTECHA1053.1, 2008.

Ackerman, S., Frey, R., Strabala, K., Liu, Y., Gumley, L., Baum, B., and Menzel, P.: Discriminating Clear-Sky From Cloud With MODIS,
440    Algorithm Theoretical Basis Document (MOD35), ATBD Version 6.1, 2010.

Althausen D., Engelmann R., Baars H., Heese B., Ansmann A., Muller D., Komppula M.: Portable Raman lidar Polly$^{XT}$ for automated profiling of aerosol backscatter, extinction, and depolarization. J.Atmos Ocean Tech 26:2366-2378. Doi10.1175/2009JTECHA1304.1, 2009.

Ansmann, A., Wandinger, U., Riebesell, M., Weitkamp, C., and Michaelis, W.: Independent measurement of extinction and backscatter
445    profiles in cirrus clouds by using a combined Raman elastic-backscatter lidar, Appl. Opt., 31, 7113-7131, 1992.

Baars, H., Ansmann, A., Engelmann, R., and Althausen, D.: Continuous monitoring of the boundary-layer top with lidar, Atmos. Chem. Phys., 8, 7281-7296, https://doi.org/10.5194/acp-8-7281-2008, 2008.

Beyerle G., Gross M. R., Haner D. A., Kjome N. T., McDermid I. S., McGee T. J., Rosen J. M.,Schafer H. J., and Schrems O., A lidar and backscatter sonde measurement campaign at Table Mountain during February-March 1997: observations of cirrus clouds, J. Atmos. Sci.
450    58, 1275-1287, 2001.

Brooks, I.: Finding Boundary Layer Top: Application of a wavelet covariance transform to lidar backscatter profiles, J. Atmos. Ocean. Tech., 20, 1092-1105, 2003.

Campbell, J. R., Vaughan, M. A., Oo, M., Holz, R. E., Lewis, J. R., and Welton, E. J.: Distinguishing cirrus cloud presence in autonomous lidar measurements, Atmos. Meas. Tech., 8, 435- 449, doi:10.5194/amt-8-435-2015, 2015.

455    Campbell, J., Lolli, S., Lewis, J., Gu, Y., and Welton, E.: Daytime Cirrus Cloud Top-of-the-Atmosphere Radiative Forcing Properties at a Midlatitude Site and Their Global Consequences, J., Appl. Meteorol. Clim., 55, 1667-1679, doi:10.1175/JAMC-D-15-0217.1, 2016.

Chen, Wei-Nai & Chiang, Chih-Wei & Nee, Jan.: Lidar Ratio and Depolarization Ratio for Cirrus Clouds. Applied optics. 41. 6470-6. 10.1364/AO.41.006470, 2002.

Comstock, J. M., Ackerman, T. P., and Mace, G. G.: Ground-based lidar and radar remote sensing of tropical cirrus clouds at Nauru Island:
460    Cloud Statistics and radiative impacts, J. Geophys. Res., 107, 4714, doi:10.1029/2002JD002203, 2002.

Das, S.K., Nee, J.B., Chiang, C.W.: A LiDAR study of the effective size of cirrus ice crystals over Chung-Li, Taiwan. J. Atmos. Terr. Phys. 72 (9-10), 781-788. http://dx.doi.org/10.1016/j.jastp.2010.03.024, 2010.

Dionisi D., Keckhut P., Liberti G. L., Cardillo F., and Congeduti F.: Midlatitude cirrus classification at Rome Tor Vergata through a multichannel Raman-Mie-Rayleigh lidar, Atmos. Chem. Phys., 13, 11853-11868, www.atmos-chem- phys.net/13/11853/2013/doi:10.5194/acp-13-
465    11853-2013 , 2013.

Dupont, J.-C., M. Haeffelin, Y. Morille, V. Noel, P. Keckhut, D. Winker, J. Comstock, P. Chervet, and A. Roblin, Macrophysical and optical properties of midlatitude cirrus clouds from four ground-based lidars and collocated CALIOP observations, J. Geophys. Res., 115, D00H24, doi:10.10294/2009JD011943, 2010.

Eloranta, E.: Practical model for the calculation of multiply scattered lidar returns, Appl. Opt., 37, 2464-2472, doi:10.1364/ao.37.002464,
470    1998.

Engelmann, R., Kanitz, T., Baars, H., Heese, B., Althausen, D., Skupin, A., Wandinger, U., Komppula, M., Stachlewska, I.S., Amiridis, V., Marinou, E., Mattis, I., Linne, H., and Ansmann, A.: The automated multiwavelength Raman polarization and water-vapor lidar Polly$^{XT}$: the neXT generation, Atmos. Meas. Tech., 9, 1767-1784, https://doi.org/10.5194/amt-9-1767- 2016, 2016.

Engelmann R., Kanitz T., Baars H., Heese B., Althausen D., Skupin A., Wandinger U., Komppula M., Stachlewska IS, Amiridis V., Marinou E., Mattis I., Linne H., Ansmann A.: EARLINET Raman lidar Polly$^{XT}$: the next generation. Atmos Meas Tech Discuss 8:7737-7780. doi10.5194/amtd-8-7737-2015, 2015.

Fernald, F.G.: Analysis of atmospheric lidar observations, some commnets, Applied Optics, vol. 32, pp. 652-653, 1984.

Filioglou, M., Nikandrova, A., Niemela, S., Baars, H., Mielonen, T., Leskinen, A., Brus, D., Romakkaniemi, S., Giannakaki, E., and Komppula, M.: Profiling water vapor mixing ratios in Finland by means of a Raman lidar, a satellite and a model, Atmos. Meas. Tech., 10, 4303-4316, https://doi.org/10.5194/amt-10-4303-2017, 2017.

Freudenthaler, V., Esselborn, M., Wiegner, M., Heese, B., Tesche, M., Ansmann, A., Muller, D., Althausen, D., Wirth, M., Andreas, F. I. X., Ehret, G., Knippertz, P., Toledano, C., Gasteiger, J., Garhammer, M., and Seefeldner, M.: Depolarization ratio profiling at several wavelengths in pure saharan dust during SAMUM 2006, Tellus B, 61, 165-179, 2009.

Garnier, A., Pelon, J., Vaughan, M. A., Winker, D. M., Trepte, C.R., and Dubuisson, P.: Lidar multiple scattering factors inferred from CALIPSO lidar and IIR retrievals of semi-transparent cirrus cloud optical depths over oceans, Atmos. Meas. Tech., 8, 2759-2774, doi:10.5194/amt-8-2759-2015, 2015.

Giannakaki, E., Balis, D. S., Amiridis, V., and Kazadzis, S.: Optical and geometrical characteristics of cirrus clouds over a Southern European lidar station, Atmos. Chem. Phys., 7, 5519-5530, doi:10.5194/acp-7-5519-2007, 2007.

Giannakaki, E., Pfuller, A., Korhonen, K., Mielonen, T., Laakso, L., Vakkari, V., Baars, H., Engelmann, R., Beukes, J. P., Van Zyl, P. G., Josipovic, M., Tiitta, P., Chiloane, K., Piketh, S., Lihavainen, H., Lehtinen, K. E. J., and Komppula, M.: One year of Raman lidar observations of free-tropospheric aerosol layers over South Africa, Atmos. Chem. Phys., 15, 5429-5442, https://doi.org/10.5194/acp-15-5429-2015, 2015.

Giannakaki, E., van Zyl, P. G., Muller, D., Balis, D., and Komppula, M.: Optical and microphysical characterization of aerosol layers over South Africa by means of multi-wavelength depolarization and Raman lidar measurements, Atmos. Chem. Phys., 16, 8109-8123, https://doi.org/10.5194/acp-16-8109-2016, 2016.

Georgousis G., Adam M., and Avdikos G.,: Signal to noise ratio estimations for a volcanic ash detection lidar. Case Study: Met Office, 27 th International Laser Radar Conference: 5-10 July, New York, USA, 2015.

Gouveia Diego A., Barja B., Barbosa H. M. J., Seifert P., Baars H., Pauliquevis T., and Artaxo P.: Optical and geometrical properties of cirrus clouds in Amazonia derived from 1 year of ground-based lidar measurements, Atmos. Chem. Phys., 17, 3619-3636, www.atmos-chem-phys.net/17/3619/2017/, doi:10.5194/acp-17-3619-2017, 2017.

He, Q. S., and Coauthors: The properties and formation of cirrus clouds over the Tibetan Plateau based on summertime lidar measurements. J. Atmos. Sci., 70, 901-915, doi:https://doi.org/10.1175/JAS-D-12-0171.1, 2013.

Hoareau, Christophe & Keckhut, Philippe & Noel, Vincent & Chepfer, H & Baray, J.: A decadal cirrus clouds climatology from ground-based and spaceborne lidars above the south of France (43.9°N-5.7°E). Atmospheric Chemistry and Physics. 13. 10.5194/acp-13-6951-2013, 2013.

Hogan, R. J. and Kew, S. F.: A 3D stochastic cloud model for investigating the radiative properties of inhomogeneous cirrus clouds, Q. J. Roy. Meteor. Soc., 131, 2585-2608, 2005. Hogan, R. J.: "Fast approximate calculation of multiply scattered lidar returns," Appl. Opt. 45, 5984-5992, 2006.

Hong, G., Yang, P., Heidinger, A. K., Pavolonis, M. J., Baum, B. A., and Platnick, S. E: Detecting opaque and nonopaque tropical upper tropospheric ice clouds: A trispectral technique based on the MODIS 8-12 $\mu$m window bands, J. Geophys. Res., 115, D20214, doi:10.1029/2010JD014004, 2010.

Illingworth, A. J., R. J. Hogan, E. J. O'Connor, D. Bouniol, M. E. Brooks, J. Delanoe, D. P. Donovan, J. D. Eastment, N. Gaussiat, J. W. F. Goddard, M. Haeffelin, H. Klein Baltink, O. A. Krasnov, J. Pelon, J.-M. Piriou, A. Protat, H. W. J. Russchenberg, A. Seifert, A. M. Tompkins, G.-J. van Zadelhoff, F. Vinit, U. Willen, D. R. Wilson and C. L. Wrench:835 Cloudnet - continuous evaluation of cloud profiles in seven operational models using ground-based observations , Bull. Am. Meteorol. Soc., 88, 883-898, 2007.

Josset, D., Pelon, J., Garnier, A., Hu, Y., Vaughan, M., Zhai, P.-W., Kuehn, R., and Lucker, P.: Cirrus optical depth and lidar ratio retrieval from combined CALIPSO-CloudSat observations using ocean surface echo, J. Geophys. Res., 117, D05207,doi:10.1029/2011JD016959, 2012.

Jylha, Kirsti & Tuomenvirta, Heikki & Ruosteenoja, Kimmo: Climate Change projections for Finland during the 21st century. Boreal Environment Research. 9, 2004.

Kienast-Sjogren, E., Rolf, C., Seifert, P., Krieger, U. K., Luo, B. P., Kramer, M., and Peter, T.: Climatological and radiative properties of midlatitude cirrus clouds derived by automatic evaluation of lidar measurements, Atmos. Chem. Phys., 16, 7605-7621, https://doi.org/10.5194/acp-16-7605-2016, 2016.

Klett, J. D.: Stable analytical inversion solution for processing lidar returns, Appl. Opt., 20, 211-220, https://doi.org/10.1364/AO.20.000211, 1981.

Kulmala, M., Asmi, A., Lappalainen, H. K., Baltensperger, U., Brenguier, J.-L., Facchini, M. C., Hansson, H.-C., Hov, O., O'Dowd, C. D., Poschl, U., Wiedensohler, A., Boers, R., Boucher, O., de Leeuw, G., Denier van der Gon, H. A. C., Feichter, J., Krejci, R., Laj, P., Lihavainen, H., Lohmann, U., McFiggans, G., Mentel, T., Pilinis, C., Riipinen, I., Schulz, M., Stohl, A., Swietlicki, E., Vignati, E., Alves, C., Amann, M., Ammann, M., Arabas, S., Artaxo, P., Baars, H., Beddows, D. C. S., Bergstrom, R., Beukes, J. P., Bilde, M., Burkhart, J. F., Canonaco, F., Clegg, S. L., Coe, H., Crumeyrolle, S., D'Anna, B., Decesari, S., Gilardoni, S., Fischer, M., Fjaeraa, A. M., Fountoukis, C., George, C., Gomes, L., Halloran, P., Hamburger, T., Harrison, R. M., Herrmann, H., Hoffmann, T., Hoose, C., Hu, M., Hyvarinen, A., Horrak, U., Iinuma, Y., Iversen, T., Josipovic, M., Kanakidou, M., Kiendler-Scharr, A., Kirkevag, A., Kiss, G., Klimont, Z., Kolmonen, P., Komppula, M., Kristjansson, J.-E., Laakso, L., Laaksonen, A., Labonnote, L., Lanz, V. A., Lehtinen, K. E. J., Rizzo, L. V., Makkonen, R., Manninen, H. E., McMeeking, G., Merikanto, J., Minikin, A., Mirme, S., Morgan, W. T., Nemitz, E., O'Donnell, D., Panwar, T. S., Pawlowska, H., Petzold, A., Pienaar, J. J., Pio, C., Plass-Duelmer, C., Prevot, A. S. H., Pryor, S., Reddington, C. L., Roberts, G., Rosenfeld, D., Schwarz, J., Seland, O., Sellegri, K., Shen, X. J., Shiraiwa, M., Siebert, H., Sierau, B., Simpson, D., Sun, J. Y., Topping, D., Tunved, P., Vaattovaara, P., Vakkari, V., Veefkind, J. P., Visschedijk, A., Vuollekoski, H., Vuolo, R., Wehner, B., Wildt, J., Woodward, S., Worsnop, D. R., van Zadelhoff, G.-J., Zardini, A. A., Zhang, K., van Zyl, P. G., Kerminen, V.-M., S Carslaw, K., and Pandis, S. N.: General overview: European Integrated project on Aerosol Cloud Climate and Air Quality interactions (EUCAARI) - integrating aerosol research from nano to global scales, Atmos. Chem. Phys., 11, 13061-13143, https://doi.org/10.5194/acp-11-13061-2011, 2011.

Komppula, M., Mielonen, T., Arola, A., Korhonen, K., Lihavainen, H., Hyvarinen, A.-P., Baars, H., Engelmann, R., Althausen, D., Ansmann, A., Muller, D., Panwar, T. S., Hooda, R. K., Sharma, V. P., Kerminen, V.-M., Lehtinen, K. E. J., and Viisanen, Y.: Technical Note: One year of Raman-lidar measurements in Gual Pahari EUCAARI site close to New Delhi in India - Seasonal characteristics of the aerosol vertical structure, Atmos. Chem. Phys., 12, 4513-4524, https://doi.org/10.5194/acp-12-4513-2012, 2012.

Laakso, L., Vakkari, V., Virkkula, A., Laakso, H., Backman, J., Kulmala, M., Beukes, J. P., van Zyl, P. G., Tiitta, P., Josipovic, M., Pienaar, J. J., Chiloane, K., Gilardoni, S., Vignati, E., Wiedensohler, A., Tuch, T., Birmili, W., Piketh, S., Collett, K., Fourie, G. D., Komppula,

M., Lihavainen, H., de Leeuw, G., and Kerminen, V.-M.: South African EUCAARI measurements: seasonal variation of trace gases and aerosol optical properties, Atmos. Chem. Phys., 12, 1847-1864, https://doi.org/10.5194/acp-12-1847-2012, 2012.

Lakkis S. Gabriela, Lavorato Mario, Canziani Pablo, Lacomi Hector, Lidar observations of cirrus clouds in Buenos Aires, Journal of Atmospheric and Solar-Terrestrial Physics, Volumes 130-131, Pages 89-95, ISSN 1364-6826, https://doi.org/10.1016/j.jastp.2015.05.020. (http://www.sciencedirect.com/science/article/pii/S1364682615001194), 2015.

Liou, K. N.: Influence of cirrus clouds on weather and climate processes: A global perspective, Mon. Weather Rev., 114, 1167-1199, 1986.

Liu, J. J., Z. Q. Li, Y. F. Zheng, and M. Cribb: Cloud-base distribution and cirrus properties based on micropulse lidar measurements at a site in southeastern China. Adv. Atmos. Sci., 32(7), 991-1004, doi: 10.1007/s00376-014-4176-2, 2015.

Lynch D. K., Sassen K., Starr D.O'C. and Stephens G.: Cirrus, ISBN: 9780195130720.

Martins, E., Noel V., and Chepfer H., Properties of cirrus and subvisible cirrus from nighttime Cloud-Aerosol Lidar with Orthogonal Polarization (CALIOP), related to atmospheric dynamics and water vapor, J. Geophys. Res., 116, D02208, doi:10.1029/2010JD014519, 2011.

Min, M., P. Wang, J. R. Campbell, X. Zong, and J. Xia: Cirrus cloud macrophysical and optical properties over north China from CALIOP measurements. Adv. Atmos. Sci., 28(3), 653-664, doi: 10.1007/s00376-010-0049-5, 2011.

Noel, Vincent & Chepfer, Helene & Ledanois, Guy & Delaval, Arnaud & Flamant, Pierre.: Classification of Particle Effective Shape Ratios in Cirrus Clouds Based on the Lidar Depolarization Ratio. Applied optics. 41. 4245-57. 10.1364/AO.41.004245, 2002.

Pandit, A. K., Gadhavi, H. S., Venkat Ratnam, M., Raghunath, K., Rao, S. V. B., and Jayaraman, A.: Long-term trend analysis and climatology of tropical cirrus clouds using 16 years of lidar data set over Southern India, Atmos. Chem. Phys., 15, 13833-13848, https://doi.org/10.5194/acp-15-13833-2015, 2015.

Platt, C. M. R.: Remote sounding of high clouds. III: Monte Carlo calculations of multiple scattered lidar returns, J. Atmos. Sci., 38, 156-167, 1981.

Reagan, J. A., X. Wang, and M. T. Osborn, Spaceborne lidar calibration from cirrus and molecular backscatter returns, IEEE Trans. Geosci. Remote Sens., 40, 2285-2290, 2002.

Reichardt, J.,: Optical and geometrical properties of northern midlatitude cirrus clouds observed with a UV Raman lidar. Phys. Chem. Earth, Part B, 24, 255-260, 1999.

Ross, K. E., Piketh, S. J., Bruintjes, R. T., Burger, R. P., Swap, R. J., and Annegarn, H. J.: Spatial and seasonal variations in CCN distribution and the aerosol-CCN relationship over southern Africa, J. Geophys. Res., 108, 8481, doi:10.1029/2002JD002384, 2003.

Sassen, K. and S. Benson, 2001: A Midlatitude Cirrus Cloud Climatology from the Facility for Atmospheric Remote Sensing. Part II: Microphysical Properties Derived from Lidar Depolarization. J. Atmos. Sci., 58, 2103-2112, https://doi.org/10.1175/1520-0469(2001)058<2103:AMCCCF>2.0.CO;2, 2001.

Sassen, K. and Cho, B. S.: Subvisual-Thin cirrus lidar dataset for satellite verification and climatological research, J. Appl. Meteorol., 31, 1275-1285, doi:10.1175/1520-0450(1992) 031<1275:STCLDF>2.0.CO 2 , 1992.

Sassen, K., Z. Wang, and D. Liu, Global distribution of cirrus clouds from CloudSat/Cloud-Aerosol Lidar and Infrared Pathfinder Satellite Observations (CALIPSO) measurements, J. Geophys. Res., 113, D00A12, doi:10.1029/2008JD009972, 2008.

Seifert, P., Ansmann, A., Muller, D., Wandinger, U., Althausen, D., Heymsfield, A. J., Massie, S. T., and Schmitt C.: Cirrus optical properties observed with lidar, radiosonde, and satellite over the tropical Indian Ocean during the aerosol-polluted northeast and clean maritime southwest monsoon, J. Geophys. Res., 112, D17205, doi:10.1029/2006JD008352, 2007.

Vaughan, M. A., Liu, Z., McGill, M. J., Hu, Y., and Obland, M. D., On the spectral dependence of backscatter from cirrus clouds: Assessing CALIOP's 1064 nm calibration assumptions using cloud physics lidar measurements, J. Geophys. Res., 115, D14206, doi:10.1029/2009JD013086, 2010.

Wandinger, U.: Multiple-scattering influuence on extinction- and backscatter-coefficient measurements with Raman and high-spectral resolution lidars, Appl. Opt., 37, 417-427, 1998.

Westbrook, C. D., and Illingworth, A. J.: Evidence that ice forms primarily in supercooled liquid clouds at temperatures > -27°C, Geophys. Res. Lett., 38, L14808, doi:10.1029/2011GL048021, 2011.

Young, S. A. and Vaughan, M. A.: The Retrieval of Profiles of Particulate Extinction from Cloud-Aerosol Lidar Infrared Pathfinder Satellite Observations (CALIPSO) Data: Algorithm Description, J. Atmospheric Ocean. Technol., 26, 1105-1119,doi:10.1175/2008JTECHA1221.1, 2009.

Young, S. A., Vaughan, M. A., Kuehn, R. E., and Winker, D. M.: The Retrieval of Profiles of Particulate Extinction from Cloud-Aerosol Lidar and Infrared Pathfinder Satellite Observations (CALIPSO) Data: Uncertainty and Error Sensitivity Analyses, J. Atmospheric Ocean. Technol., 30, 395-428, doi:10.1175/JTECH-D-12-00046.1, 2013.

Young, S. A., Vaughan, M. A., Garnier, A., Tackett, J. L., Lambeth, J. D., and Powell, K. A.: Extinction and optical depth retrievals for CALIPSO's Version 4 data release, Atmos. Meas. Tech., 11, 5701-5727, https://doi.org/10.5194/amt-11-5701-2018, 2018.

**Table 1.** Technical specifications of the Polly$^{XT}$ System.

| Characteristics | Polly$^{XT}$ |
|---|---|
| Operating Wavelength(s) | 355nm, 532nm, 1064nm |
| Average pulse energy | ~450 mJ |
| Laser beam divergence | <0.2 mrad |
| Telescope diameter | 0.3m |
| Receiver field of view | 1mrad |
| Detectors | Hamamatsu PMTs |
| Polarization | Cross & Total |
| Raw data range resolution | 30m |
| Raw data time resolution | 30s |

**Table 2.** Average cirrus properties for the three regions for daytime and nighttime measurements.

| Cirrus Properties | Gual Pahari | Elandsfontein | Kuopio |
|---|---|---|---|
| Cirrus Base (m) | $9000 \pm 1580$ | $9200 \pm 810$ | $8600 \pm 1080$ |
| | $8900 \pm 1480$ d | $9200 \pm 818$ d | $8037 \pm 914$ d |
| | $9000 \pm 1529$ n | $9200 \pm 744$ n | $7900 \pm 1246$ n |
| Cirrus Top (m) | $10600 \pm 1800$ | $10826 \pm 906$ | $9800 \pm 1075$ |
| | $10350 \pm 2000$ d | $10705 \pm 928$ d | $9443 \pm 1095$ d |
| | $10900 \pm 1700$ n | $10889 \pm 928$ n | $8965 \pm 1055$ n |
| Cirrus geometrical thickness (m) | $1500 \pm 700$ | $1600 \pm 735$ | $1200 \pm 700$ |
| | $1480 \pm 700$ d | $1627 \pm 802$ d | $1167 \pm 700$ d |
| | $1300 \pm 638$ n | $1696 \pm 616$ n | $1243 \pm 700$ n |
| Temperature base (C) | $-33 \pm 6$ | $-34 \pm 5$ | $-43 \pm 10$ |
| Temperature top (C) | $-45 \pm 4$ | $-45 \pm 6$ | $-57 \pm 9$ |

**Table 3.** Average cirrus optical properties for the three regions for daytime and nighttime measurements.

| Cirrus Properties | Gual Pahari | Elandsfontein | Kuopio |
|---|---|---|---|
| N | 11 (7d, 4n) | 64 (32d, 32n) | 213 (153d, 50n) |
| % subvisible | 0 | 2 | 3 |
| % thin | 20 | 61 | 71 |
| % opaque | 80 | 37 | 26 |
| LR 355 | $27 \pm 12$ | $26 \pm 6$ | $33 \pm 7$ |
| | $23 \pm 8$ d | $24 \pm 7$ d | $33 \pm 7$ d |
| | $31 \pm 15$ n | $27 \pm 8$ n | $33 \pm 7$ n |
| LR 532 | $28 \pm 22$ | $25 \pm 6$ | $31 \pm 7$ |
| | $23 \pm 3$ d | $24 \pm 5$ d | $31 \pm 7$ d |
| | $33 \pm 11$ n | $26 \pm 7$ n | $30 \pm 7$ n |
| COD 355 | $0.60 \pm 0.25$ | $0.35 \pm 0.30$ | $0.25 \pm 0.20$ |
| | $0.40 \pm 0.30$ d | $0.34 \pm 0.30$ d | $0.24 \pm 0.21$ d |
| | $0.80 \pm 0.20$ n | $0.36 \pm 0.30$ n | $0.26 \pm 0.20$ n |
| COD 532 | $0.45 \pm 0.30$ | $0.30 \pm 0.30$ | $0.24 \pm 0.20$ |
| | $0.30 \pm 0.40$ d | $0.25 \pm 0.30$ d | $0.26 \pm 0.20$ d |
| | $0.60 \pm 0.20$ n | $0.35 \pm 0.30$ n | $0.22 \pm 0.20$ n |
| CR (355/532) | $1.50 \pm 0.80$ | $1.40 \pm 1.10$ | $1.10 \pm 0.80$ |

**Table 4.** Predominant aerosol type and AOD FT for the three regions.

| Measurement Site | Gual Pahari | Elandsfontein | Kuopio |
|---|---|---|---|
| Predominant aerosol type | dust particles , biomass burning | biomass burning, desert dust particles and urban particles | fine particles |
| AOD FT | $0.09 \pm 0.03$ | $0.06 \pm 0.04$ | $0.01 \pm 0.01$ |
| COD | $0.60 \pm 0.25$ | $0.35 \pm 0.30$ | $0.25 \pm 0.20$ |

**Table 5.** Summary of cirrus clouds geometrical and optical properties of ground-based lidar observations reported in literature.

| Measurement site | Location | Cirrus Base (km) | Cirrus Top (km) | LR (sr) | COD | Reference |
|---|---|---|---|---|---|---|
| Kuopio | 62.74°N, 27.54°E | 8.0 ± 1.1 | 9.3 ± 1.1 | 33 ± 7 | 0.25 ± 0.20 | This Study |
| France | 43.9°N, 5.7°E | 9.3 ± 1.8 | 10.9 ± 1.7 | | | Hoareau et al., 2013 |
| Rome | 41.8°N, 12.6°E | | | 31 ± 15 | 0.37 ± 0.18 (532nm) | Dionisi et al., 2013 |
| Thessaloniki | 40.6°N, 22.9°E | 8.8 ± 1.0 | 10.3 ± 0.9 | 30 ± 17 | 0.31 ± 0.24 (355nm) | Giannakaki et al., 2007 |
| Naqu | 31.5°N, 92.1°E | 13.7 ± 2 | 15.6 ± 1.6 | 28 ± 15 | 0.33 ± 0.29 (532nm) | He et al., 2013 |
| Gual Pahari | 28.43°N, 77.15°E | 9.0 ± 1.6 | 10.6 ± 1.8 | 27±12 | 0.59 ± 0.39(355nm) | This Study |
| Gadanki | 13.5°N, 79.2°E | 13.0 ± 2.2 | 15.3 ± 2.0 | | | Pandit et al., 2015 |
| Hulule | 4.1°N, 73.3°E | 12 ± 1.6 | 13.7 ± 1.4 | 32 | 0.28 (532nm) | Seifert et al., 2007 |
| Amazonia | 2.89°S, 59.97°W | 12.9 ± 2 | 14.3 ± 1.9 | 23 ± 8 | 0.25 ± 0.46 (355nm) | Gouveia et al., 2017 |
| La Reunion | 20.8°S, 55.5°W | | 13.0 | | 0.05 | Hoareau et al., 2012 |
| Elandsfontein | 26.25°S, 29.43°E | 9.2 ± 0.8 | 11 ± 0.9 | 26 ± 6 | 0.35 ± 0.30 | This Study |
| Buenos Aires | 34.6°S, 58.5°W | 9.6 | 11.8 | | 0.26 ± 0.11 | Lakkis et al., 2015 |
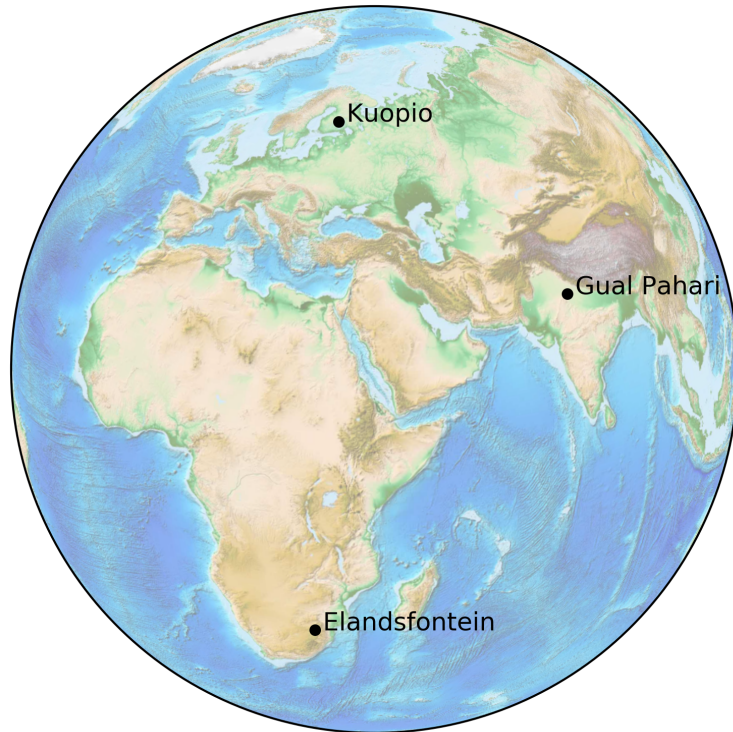
**Figure 1.** Map of the three measuring sites.
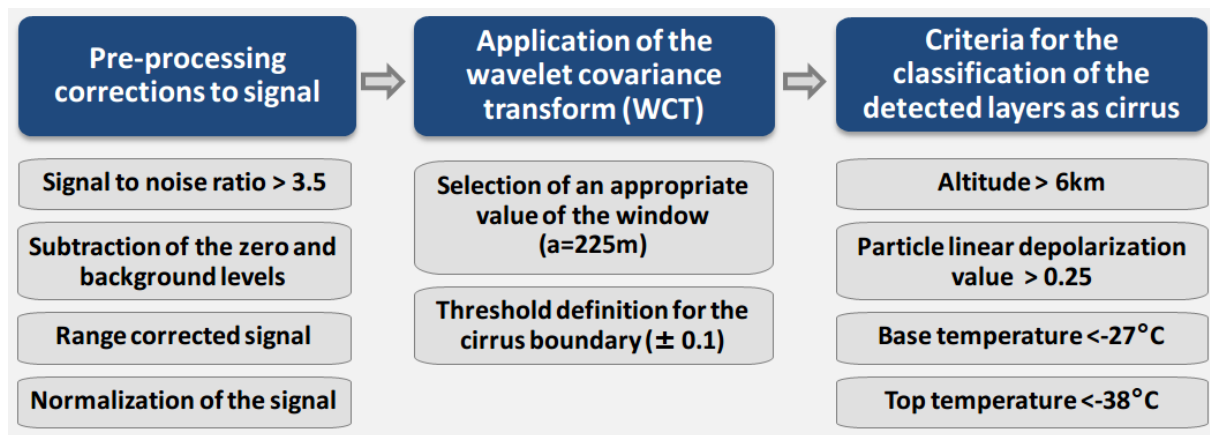
**Figure 2.** Schematic flowchart showing the main steps of the methodology applied in this study to obtain the cirrus geometrical boundaries from the Polly$^{XT}$ measurements.
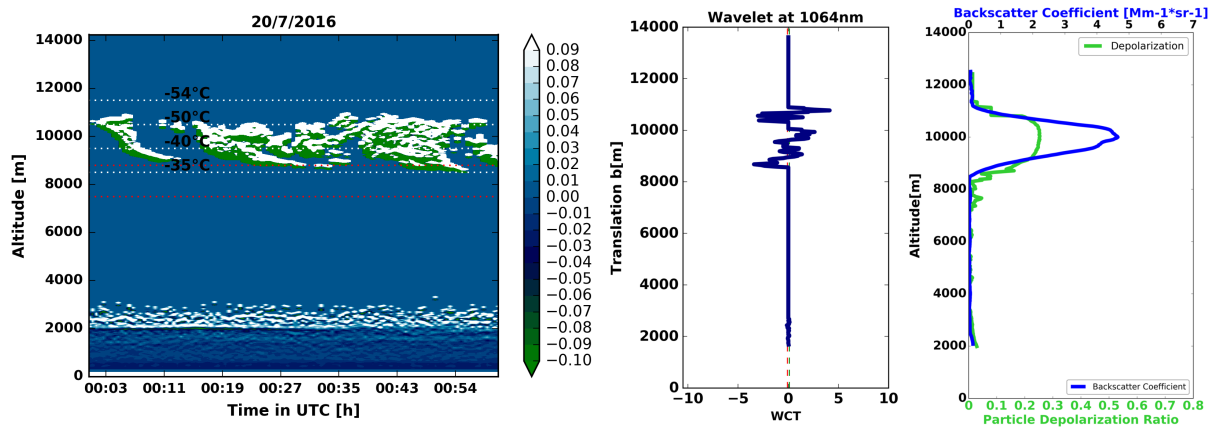
**Figure 3.** Cirrus cloud hourly evolution as determined from the Polly$^{XT}$ with temperatures values marked with white lines and the temperature criteria marked with red lines (a), the averaged WCT applied to 1064nm (b) and the mean particle depolarization ratio (green) and the backscatter coefficient profile (blue) at 532nm (c), on 20th of July 2016 at Kuopio station.
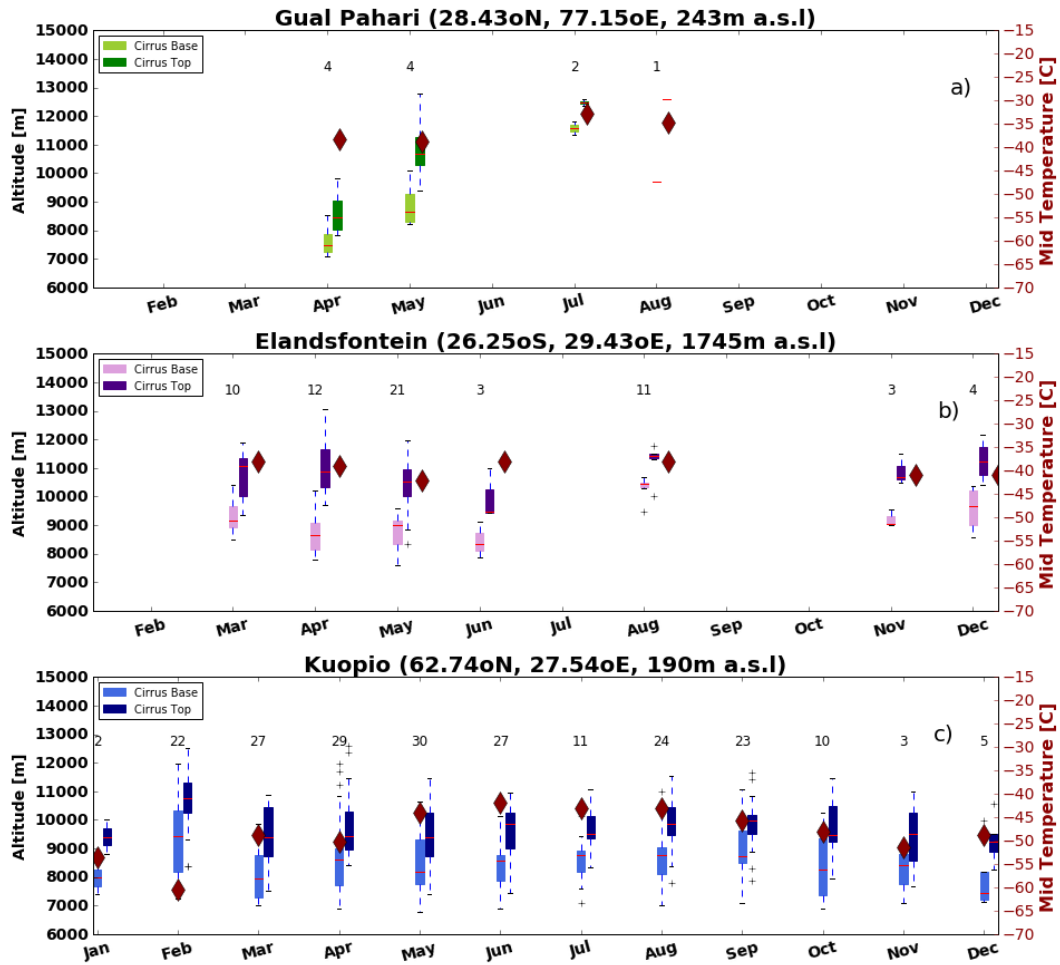
**Figure 4.** Monthly cycle of the mean cirrus base and top and the corresponding mid temperature values (rhombus) of the cirrus clouds at Gual Pahari (a), Elandsfontein (b) and Kuopio (c). Horizontal line in box: median. Boxes: the upper and lower quartile. Whisker: extreme values. Numbers labeled indicate the number of cirrus cases per month.
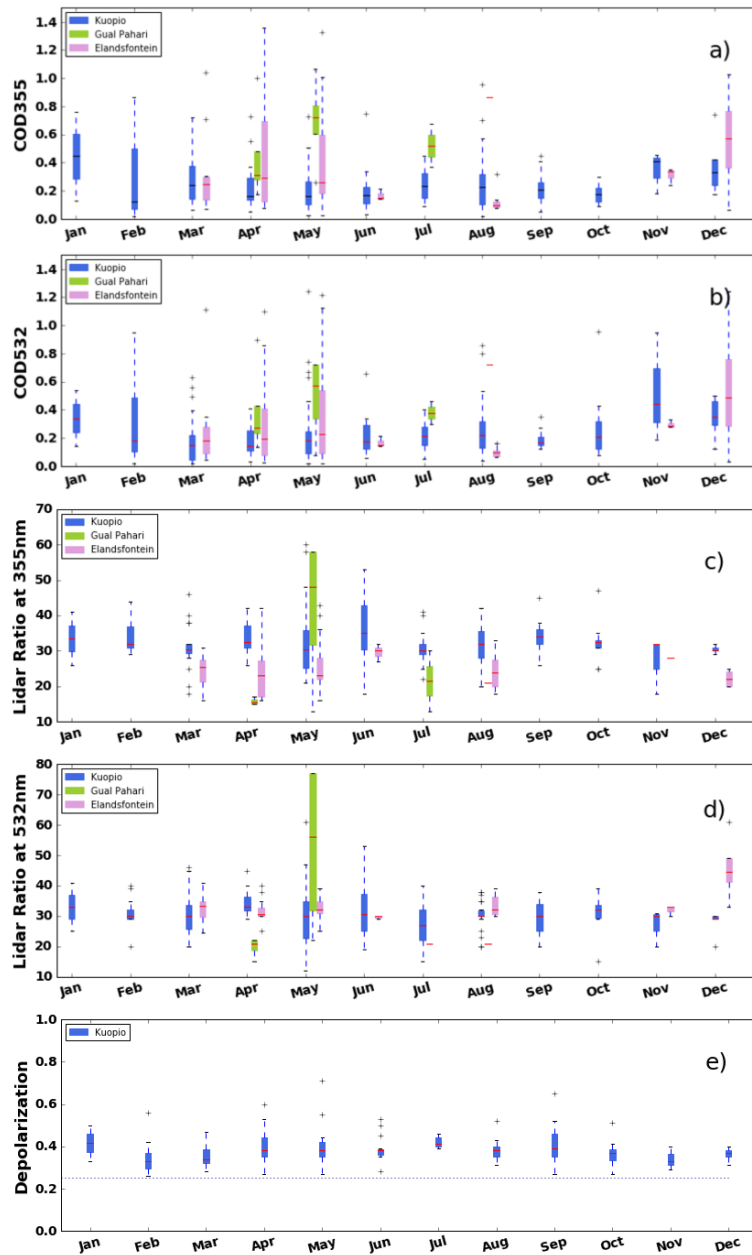
**Figure 5.** Mean optical depth (multiple scattering corrected) values at 355nm (a), mean optical depth (multiple scattering corrected) values at 532nm (b), Lidar ratio at 355nm (c), Lidar ratio at 532nm (d) and particle depolarization ratio (e) for the detected cirrus layers for the study period for the three regions. Horizontal line in box: median. Boxes: the upper and lower quartile. Whisker: extreme values. Red line stands for the mean values for every month.
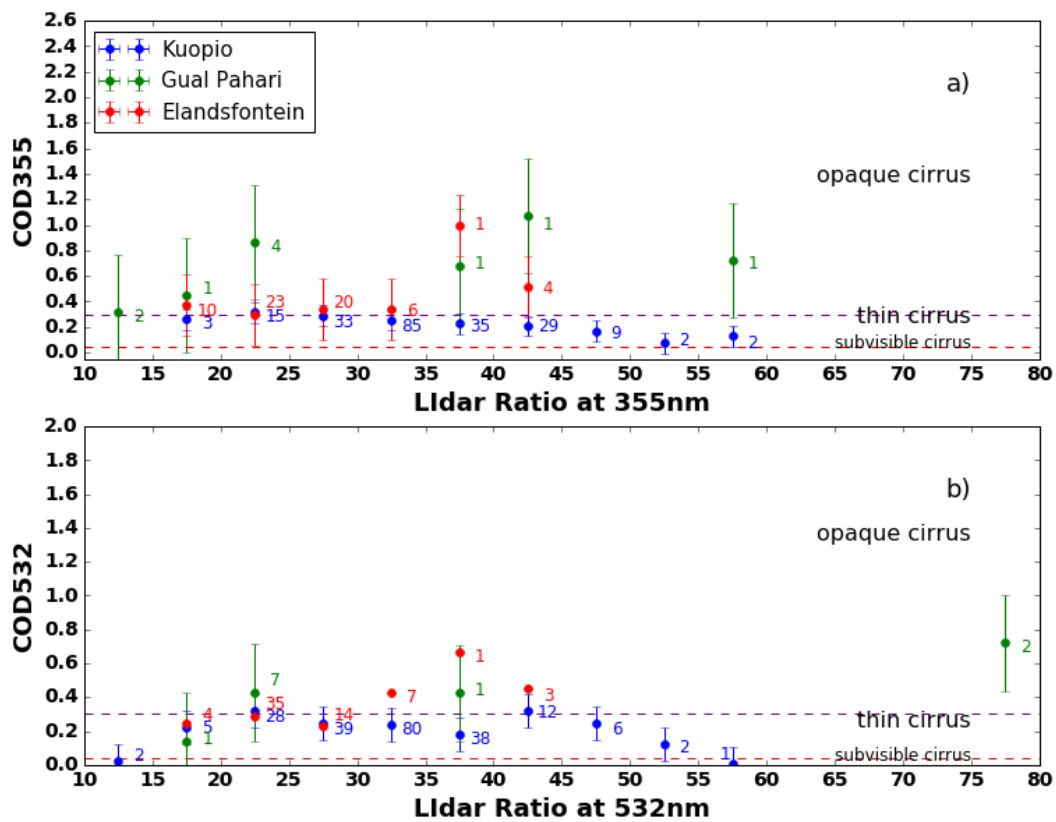
**Figure 6.** Dependence of the Lidar ratio with COD at 355nm (a) and the Lidar ratio with COD at 532nm (b). Numbers labeled indicate the number of cases per lidar ratio bin. Horizontal dashed lines: cirrus categories by Sassen and Cho (1992).
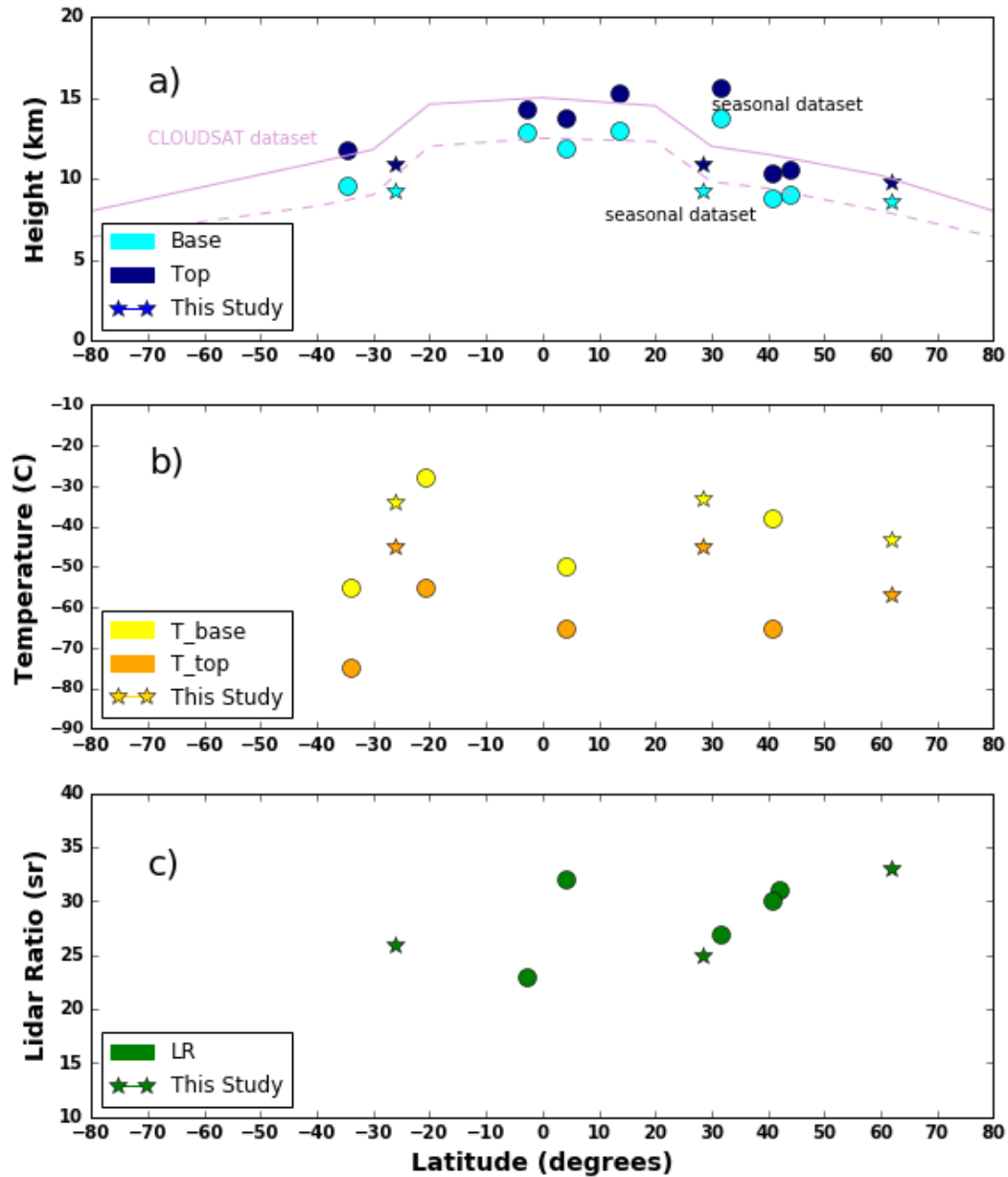
**Figure 7.** Latitudinal dependence of cirrus base and top height. Circles denote estimations from groundbased lidar from the literature (see Table 5 for references), stars denote estimations from this study and lines correspond to CLOUDSAT estimations according to Sassen et al. (2008) (a), latitudinal dependence of cirrus temperature base and top. Circles denote estimations from groundbased lidar from the literature (see Table 5 for references), stars denote estimations from this study (b) and same as above, but for latitudinal dependence of Lidar ratio values (c).
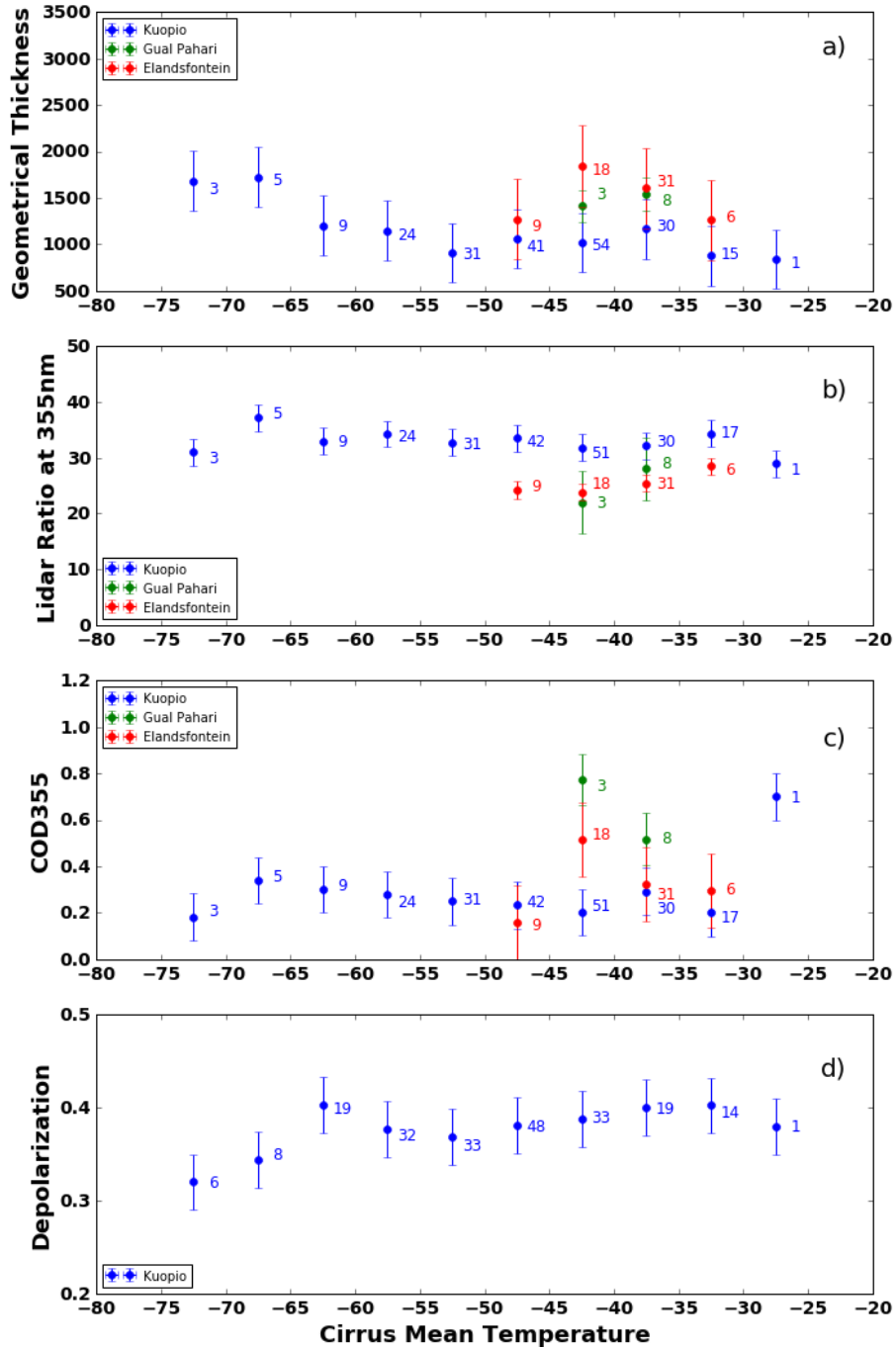
**Figure 8.** Dependencies of cirrus geometrical thickness (a), Lidar ratio at 355nm (b), optical depth at 355nm (c) and particle depolarization values (d) on 5°C intervals of cirrus mid temperature. Numbers labeled indicate the number of cases per temperature bin.
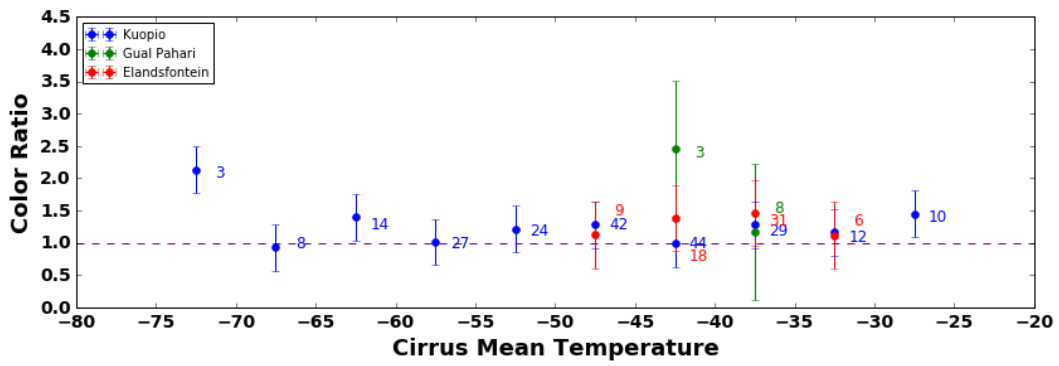
**Figure 9.** Dependencies of color ratio (355/532) on 5°C intervals of cirrus mid temperature. Numbers labeled indicate the number of cases per temperature bin.
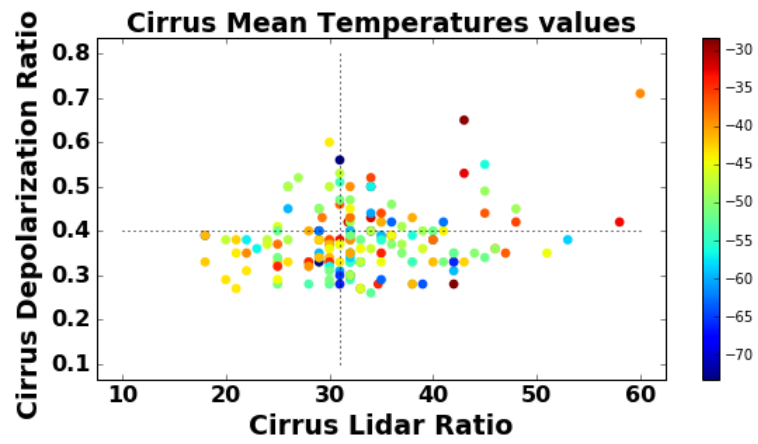
**Figure 10.** Dependencies of the mean temperature with the Lidar ratio values at 355nm and the particle depolarization values.